



## Nano-Devitrification and Structural Evolution of Rapidly Solidified Amorphous Al-TM (Cu-Co)-Y (at.%) Alloy

M. Salehi\*, S.G. Shabestari, M. Dadashi

School of Metallurgy and Materials Engineering, Iran University of Science and Technology (IUST), Tehran, Iran.

Received: 2 October 2021; Accepted: 26 November 2021

\*Corresponding author email: [maryamsalehi@iust.ac.ir](mailto:maryamsalehi@iust.ac.ir)

### ABSTRACT

Activation energies and other kinetic parameters of primary crystallization of  $Al_{86}Cu_6Co_2Y_6$  (at.%) amorphous alloy describing the mechanism was determined. Melt spinning on a child copper wheel was used to prepare the  $Al_{86}Cu_6Co_2Y_6$  (at. %) amorphous ribbons. The ribbons at as-spun and annealed conditions were studied by optical microscopy (OM), differential scanning calorimetry (DSC), X-ray diffraction and field emission scanning electron microscopy (FESEM). The kinetic parameters of the crystallization process were determined by Kissinger and Moynihan methods at non-isothermal condition. Crystallization mechanism was studied using the Johnson–Mehl–Avrami equation. According to the average value of Avrami exponent ( $2.065 \pm 0.16$ ), the primary crystallization process is conducted by 3D diffusional growth with decreasing rate. The  $\alpha$ -Al nanoparticles below 50 nm in size distributed evenly in the glassy matrix and intermetallic phases ( $Al_3Y$ ,  $AlCu_3$  and  $Al_{11}Y_3$ ) were formed during the first and second stages of crystallization, respectively.

**Keywords:** Aluminum alloy, Rapid solidification, Metallic glass, Nanocrystal, Crystallization

### 1. Introduction

During the past years rapidly solidified (RS) aluminum alloys due to the ability of the process to fabricate metallic glasses with better physical and mechanical properties have attracted considerable attention which makes them promising candidates as advanced engineering materials for fundamental research and numerous industrial applications [1-5].

Aluminum (high content) based metallic glasses with transition metal (TM) and rare earth (RE) combination have been studied intensively due to their high glass forming ability (GFA) and mechanical properties. The high tensile strength (up to 1000 MPa) which is about twice as high as that of conventional high-strength aluminum alloys can be obtained. Partial crystallization of the amorphous alloys which leads to precipitate the fcc-

Al nanocrystals homogeneously in the amorphous matrix can enhance even more the mechanical properties [6-12].

The amorphous-to-crystalline transformation has been intensively studied over the past two decades in which generally three types of crystallization were classified for amorphous alloys: polymorphous, eutectic and primary [13]. An important method to control the production of nanocomposite materials is primary devitrification of the amorphous matrix [14]. The high strength of nanocrystalline alloys has been attributed to different mechanisms. The enhancement of the shear bands number and suppressing propagation of them leads to structural heterogeneities in the amorphous matrix and improvement of plasticity. Therefore, the ductility noticeably improves and

deformation occurs homogeneously [15-17]. Moreover, increasing the solute content of the remaining amorphous matrix after nanocrystals formation, or the influence of both nanocrystals of  $\alpha$ -Al phase and the amorphous matrix have contributed to higher strength of the alloy. These amorphous-nanocrystalline composites become brittle if the precipitated phases are intermetallic compounds. In the other word, it is also known that the crystallization of intermetallic at higher temperatures produces a deleterious effect on the properties of the alloys [10]. Therefore, making the evaluation of GFA, thermal stability and control the primary crystallization of the Al-based metallic glass alloys are extremely important [18,19]. Studying the crystallization kinetics of the amorphous alloys and their controlled crystallization are crucial in order to produce desirable microstructures which improves the mechanical properties.

The aim of the present investigation is to evaluate GFA, thermal stability and crystallization behaviour of the melt-spun ribbons in non-isothermal condition. In addition, the effect of different nanocrystalline phases which crystallized during each reaction step of the  $\text{Al}_{86}\text{Cu}_6\text{Y}_6\text{Co}_2$  (at.%) amorphous alloy has been investigated. The activation energies have been calculated by different methods to describe the mechanism of the nucleation and growth.

## 2. Experimental details

High frequency induction melting was applied to prepare the alloy ingot with nominal composition of  $\text{Al}_{86}\text{Cu}_6\text{Co}_2\text{Y}_6$  (at.%) using 99.97% purity Al, 99.98% purity Cu and 99.9% purity Y and Co under an argon atmosphere. The ingot was remelted for three times to obtain homogeneous composition. In the melt spinning process, molten alloy was poured onto a cylindrical surface of a copper wheel with 32 cm diameter and rotating speed of about 40  $\text{ms}^{-1}$ . The ribbons with typical dimensions of 15-22  $\mu\text{m}$  thick, 1-1.5 mm wide, and up to several meters long have been produced. The crystallization behavior of the amorphous ribbons was studied by differential scanning calorimetry (DSC- Mettler Toledo). Structural evaluation was studied by field emission electron microscopy (KYKY-EM 8000F (FE-SEM)) and X-ray diffraction (XRD-Philips, PW1800, Cu-K $\alpha$  ( $\lambda = 1.54 \text{ \AA}$ ) radiation, 40 kV and 20 mA) at  $2\theta$  range from  $10^\circ$  to  $80^\circ$ . The FE-SEM operated at a voltage of 15 kV and was linked with an energy dispersive spectrometry (EDS Silicon

Drift 2017) attachment. Standard metallographic techniques were used in order to study the structural investigations. This was followed by chemical etching in a modified Keller's solution for about 5 s. The resultant cross-sectional microstructures of the melt-spun specimen was characterized by a Neophot 32 optical microscope.

## 3. Results and discussion

### 3.1. Structural analysis

Referring to Fig. 1a, XRD pattern of the as-spun  $\text{Al}_{86}\text{Cu}_6\text{Co}_2\text{Y}_6$  (at.%) alloy shows a wide peak at the  $2\theta$  range of  $32\text{--}48^\circ$  with a fully amorphous structure. No long range atomic order can be seen in the amorphous metallic alloys compared to the crystalline structure with a lattice periodicity. Liquid-like atomic structure of the alloying constituents is maintained during the rapid solidification of the liquid and a metastable glass-like structure forms [20].

Fig. 2 presents the DSC plots of the melt-spun  $\text{Al}_{86}\text{Cu}_6\text{Co}_2\text{Y}_6$  alloy at 10, 20 and 30  $\text{Kmin}^{-1}$  heating rates. From the DSC curves, there is an endothermic peak, glass transition to supercooled liquid temperature  $T_g$ , which is followed by two exothermic peaks related to two crystallization steps. All transition temperatures in the DSC curve move to higher temperatures and their intensity increases as the heating rate increases due to the thermally activated crystallization process.

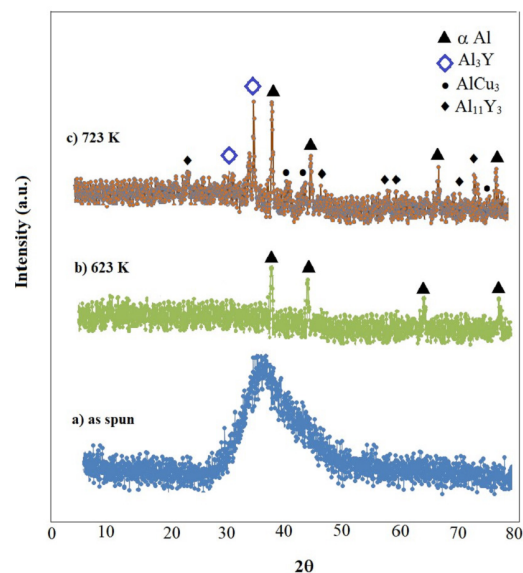


Fig. 1- XRD patterns of (a) the as-spun  $\text{Al}_{86}\text{Cu}_6\text{Co}_2\text{Y}_6$  ribbons and (b-c) the non- isothermally annealed ribbons up to the end temperatures of each crystallization reaction.

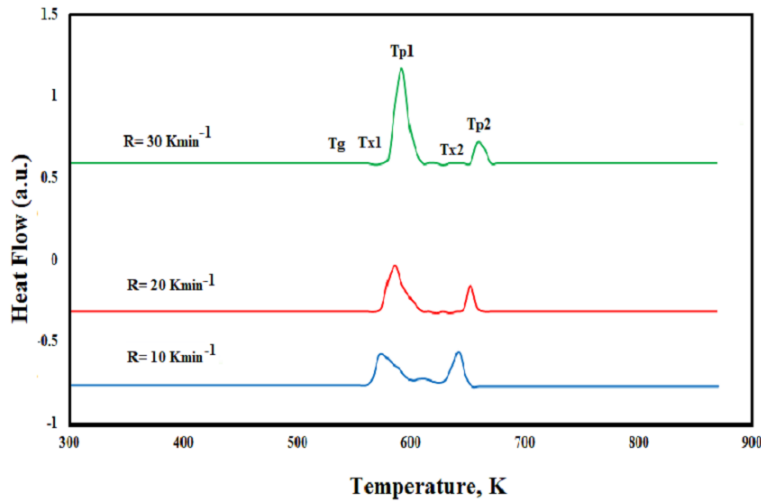


Fig. 2- DSC curves of  $Al_{86}Cu_6Co_2Y_6$  amorphous alloy at different rates of heating.

According to the DSC curves, the glass transition temperature, crystallization onset temperatures ( $T_{X1}$ ,  $T_{X2}$ ) and the first peak temperature  $T_{P1}$  of the alloy for heating rates of  $20\text{ Kmin}^{-1}$  are 552 K, 576 K, 769 K and 584 K, respectively. The present melt spun ribbons show more transition temperatures with respect to the  $Al_{86}Ni_6Y_6Ce_2$  ribbons with fully amorphous structure and the same Al atomic percent, and it is also comparable to  $Al_{84}Ni_6Y_6Ce_4$  glassy alloy [16] indicating high thermal stability of the studied ribbons.

The significant mismatch in the atomic radius of the constituents and their heat of mixing with high negative values leads to complexity of the system and enhancement of the onset crystallization temperature (576 K) of the studied alloy. The enhancement of GFA in the Al-Co-Cu-Y alloy system can be interpreted through the Inoue criteria [21]. The values of mixing enthalpy and atomic size of the elements of AlCoCuY alloy system are presented in Fig. 3. Y has the largest atomic radius in the system that leads to significant atomic size mismatch, and the interplay between large atoms of Y and other smaller atoms. As the radius of Cu is similar to that of Co, it influences no change in order of the atomic size, such that  $Y > Al > Co = Cu$ . Large Y atoms with high melting temperature decrease the diffusion coefficient of the atoms [18]. Therefore, movement of the atoms becomes more difficult and the melt tends to keep the amorphous structure. Moreover, the significant negative mixing enthalpy among the ingredients of the alloy system affects the GFA. The positive mixing enthalpy of the Cu and Co ( $\Delta H_{Cu-Co\text{ mix}}$ ) decreases

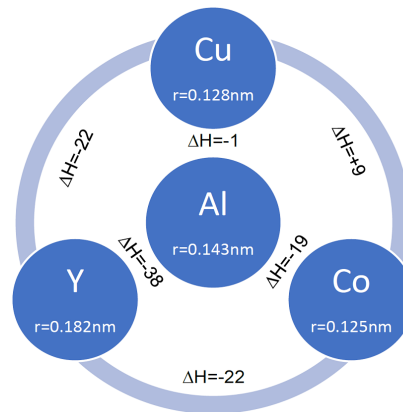


Fig. 3- The atomic radius and mixing enthalpy of the constituent elements of the AlCoCuY alloy system.

the mixing enthalpy of the. The significant negative mixing enthalpy between Y with Cu ( $\Delta H_{Cu-Y\text{ mix}}$ ), with Co ( $\Delta H_{Y-Co\text{ mix}}$ ) and with Al ( $\Delta H_{Y-Al\text{ mix}}$ ) results in atomic interactions and presence of short-range arrangement of atoms in the undercooled liquid, which causes to increases the atomic packing efficiency, and diminish the diffusion and ordering of atoms in the long-range.

Glass forming ability and the thermal stability of alloy systems can be evaluated by many proposed criteria. It is clearly found that the stability of the supercooled liquid has an important effect on the GFA and the thermal stability of an alloy [22]. In this research, the maximum width of the supercooled liquid region,  $\Delta T_{X1}$  ( $T_{X1} - T_g$ ), is 26 corresponding to the  $10\text{ Kmin}^{-1}$  heating rate. High  $\Delta T_x$  implies better GFA [18,19]. However, the  $\Delta T_x$  of the bulk metallic glasses is larger than 50 K, this

is mostly less than 30 K in the Al-based amorphous alloys. Figs. 1b and 1c show the XRD results of the  $Al_{86}Cu_6Co_2Y_6$  (at.%) ribbons which are isochronal heated to the end temperatures of each DSC peaks at 20  $Kmin^{-1}$  heating rate. According to the XRD analysis, fcc  $\alpha$ -Al crystals are formed from the amorphous matrix during the first exothermic reaction (Fig. 1b). Broad Al peaks in the XRD patterns implies the small grain size. The grain size (d), about 31.8 nm, was determined using the following equation [16]:

$$D = \frac{k \lambda}{\beta \cos \theta} \quad (1)$$

In this equation, K is the shape factor ( $\approx 0.97$ ),  $\beta$  the peak broadening,  $\theta$  the diffraction angle and  $\lambda$  is the wavelength. Devitrification induced by annealing leads to presence  $Al_3Y$ ,  $AlCu_3$  and  $Al_{11}Y_3$  phases and some undefined phases observed for 723 K (Fig. 1c) in the next reaction step. Complex intermetallic phases are formed along the nanocrystalline fcc  $\alpha$ -Al during the second crystallization step and the width and intensity of  $\alpha$ -Al peaks increases implying the growth of  $\alpha$ -Al phase. However, it should be considered that equation (1) has limitations and XRD patterns do not give a precise calculation of the crystal size. It only provides an order of magnitude for nano-sized crystals. Instrumental broadening must be taken into account

Table 1- Lattice constant of fcc-Al of  $Al_{86}Cu_6Co_2Y_6$  alloy

$2\theta$ (degree)	h k l	a (nm)
38.26	111	0/407125
44.49	200	0/406955
64.91	210	0/405998
77.95	220	0/40618

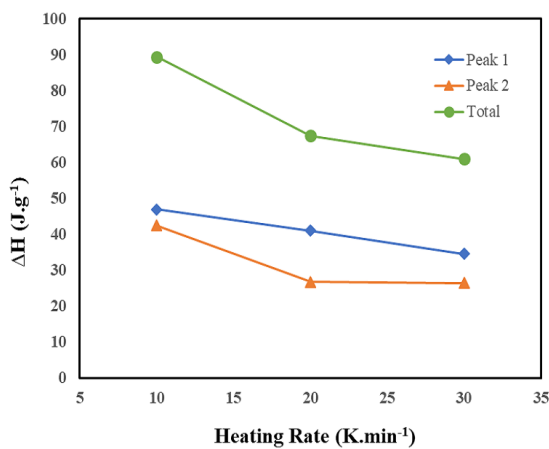


Fig. 4- The crystallization enthalpies of  $Al_{86}Cu_6Co_2Y_6$  alloy at different heating rates.

in the case of bigger crystallites.

Lattice constants of fcc-Al calculated from the XRD traces (Fig. 1b) are listed in Table 1. Referring to the obtained XRD pattern, the Al (1 1 1), (2 0 0), (2 1 0) and (2 2 0) line shifts yield the lattice parameter value of about 0.4066 nm for the annealed ribbons which is higher than the 0.4050 nm of pure Al. Therefore, increasing cooling rate leads to enhancement of the lattice parameter as the result of high supersaturation of the solute elements to fcc-Al. Y with atomic size of 0.182 nm, is much larger than that of the Al of 0.143 nm. It seems that lattice constant improvement is related to the higher supersaturation of Y as the atomic radius of Cu and Co are smaller than that of Al. Therefore, the melt spinning process leads to an increase in the solubility of the Al matrix during rapid solidification and the primary crystallization of intermetallic phases is avoided.

The total crystallization enthalpy and enthalpy of each crystallization step which is calculated by integrating the area under the DSC curve, was also measured and shown in Fig. 4. The enthalpies corresponding to the first, second and total crystallization enthalpies are -28, -42 and  $-70 Jg^{-1}$ , respectively for the amorphous ribbon at the 20  $Kmin^{-1}$  heating rate. It can be seen the primary crystallization enthalpy of  $\alpha$ -Al is more than the value for intermetallic formation during the second step.

The microstructures of the cross-sectional of ribbons are shown in Fig. 5. Solute enrichment ahead of the solidification interface occurs due to the constitutional supercooling. It is also well defined that solute pileup due to insufficient time for diffusion or solute redistribution and

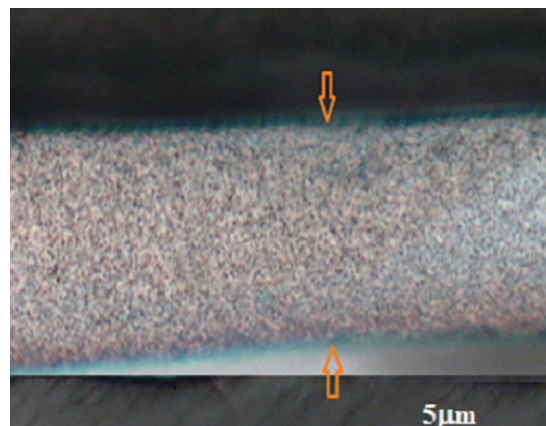


Fig. 5- Optical micrograph of the melt-spun  $Al_{86}Cu_6Co_2Y_6$  ribbons.

crystallization is an important concern in the case of rapid solidification processes such as melt spinning, [3]. Moreover, there is any visible crystal which confirms the amorphous structure of the alloy.

Fig. 6 shows FE-SEM images of as-spun amorphous  $Al_{86}Cu_6Y_6Co_2$  (at. %) alloy and ribbons continuously heated to the end temperature of the first exothermic peak (623 K). According to the XRD analysis (Fig. 1b), fcc-Al phase is formed in this temperature. Fig. 6a shows the amorphous microstructure of the melt-spun ribbon which is in accordance with the XRD result shown in Fig. 1a. The absence of any visible crystal in the microstructure confirms also the amorphous structure. Fig. 6b shows the  $Al_{86}Cu_6Y_6Co_2$  amorphous alloy continuously heated to 623 K with corresponding EDS pattern. The nanometer scale of  $\alpha$ -Al crystals with size below 50 nm are dispersed in the as-spun glassy matrix. The EDS pattern confirms the precipitation of the  $\alpha$ -Al phase in the matrix. Even though EDS analysis is rather inaccurate for small phases due to the effect of matrix composition in the EDS analysis of nanoparticles, the fine bright phases have been considered to be fcc  $\alpha$ -Al crystals. Y atoms which have large and slow diffusing nature at the crystal growth fronts result in inhibition of crystal growth rates. Therefore, they form nanostructured composite of fcc-Al crystallites in the glassy matrix. In other words, the nanocrystalline-amorphous composite material can be obtained by heating at this temperature.

### 3.2. Kinetics of crystallization

#### 3.2.1. Calculation of activation energy

Activation energy  $E_a$  of the crystallization can be applied to determine the thermal stability of metallic glasses which can be calculated by different methods [23-26] including Moynihan and Kissinger methods:

$$\ln(\beta) = \left(-\frac{E_a}{RT_p}\right) + C \quad (\text{Moynihan}) \quad (2)$$

$$\ln\left(\frac{\beta}{T_p^2}\right) = \left(-\frac{E_a}{RT_p}\right) + C \quad (\text{Kissinger}) \quad (3)$$

Where  $\beta$  is the heating rate,  $T_p$  is the crystallization peak,  $E_a$  is the apparent activation energy,  $R$  is the gas constant ( $8.314 \text{ J K}^{-1} \text{ mol}^{-1}$ ) and  $C$  is a constant. Fig. 7a and 7b show the Moynihan and Kissinger plots for the first and second crystallization of  $Al_{86}Cu_6Y_6Co_2$  amorphous alloy respectively which displays excellent linearity. Table 2 reports the activation energies  $E_{a1}$  of crystallization calculated from the slope of the straight lines at 10, 20 and 30  $\text{K min}^{-1}$  heating rates. It is important to note that the results of Moynihan method ( $183.1 \pm 12.4 \text{ kJ mol}^{-1}$ ) and Kissinger method ( $173.4 \pm 10.7 \text{ kJ mol}^{-1}$ ) are close to each other which imply the unity of the reaction order.

Table 2- The activation energies calculated by Moynihan and Kissinger methods for  $Al_{86}Cu_6Y_6Co_2$  alloy

Devitrification	Moynihan $\text{kJ mol}^{-1}$	Kissinger $\text{kJ mol}^{-1}$
$T_{p1}$	$183.1 \pm 12.4$	$173.4 \pm 10.7$
$T_{p2}$	$185.6 \pm 9.6$	$184.3 \pm 14.1$

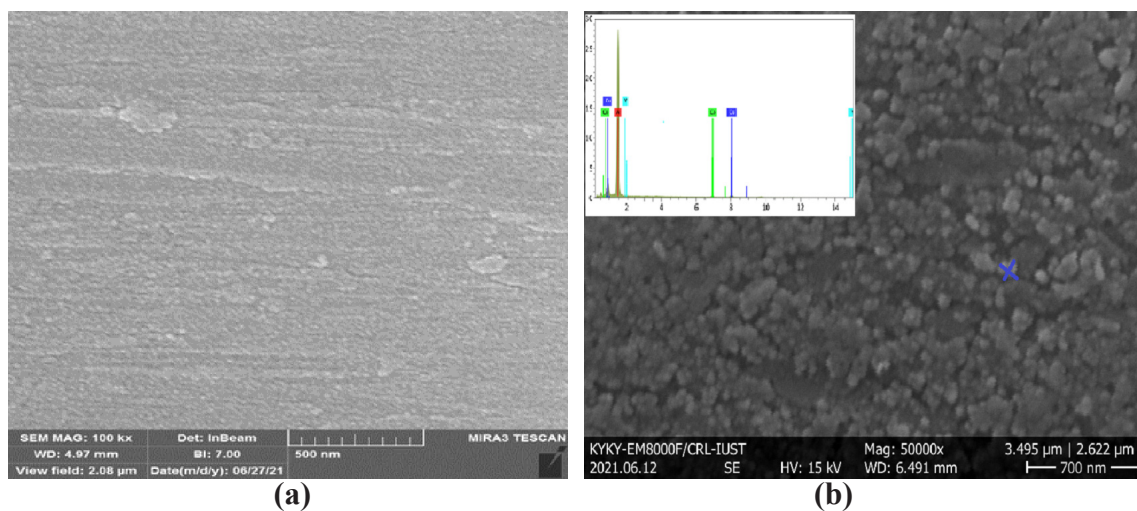


Fig. 6- FE-SEM image of the  $Al_{86}Cu_6Y_6Co_2$  (at. %) alloy for (a) as-spun ribbons and (b) ribbons annealed at 623 K (at the end position of the first peak temperature) with corresponding EDS pattern of selected nanocrystal precipitated.

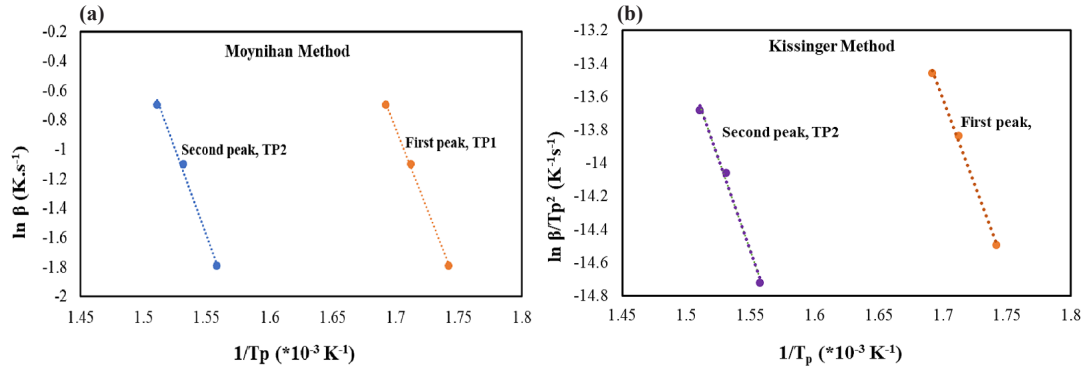
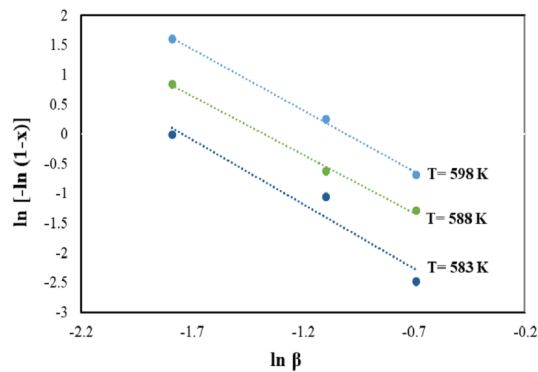
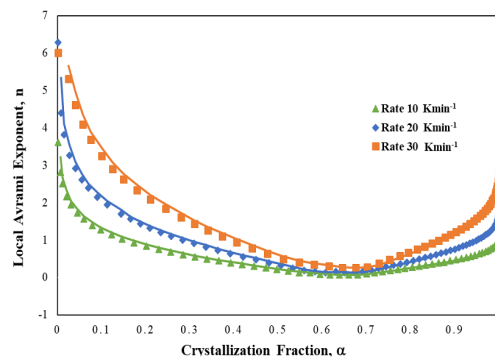


Fig. 7- (a) Moynihan plot and (b) Kissinger plot for the first and second crystallization processes at various temperatures.

Fig. 8- Plots of JMA equation of Al<sub>86</sub>Cu<sub>6</sub>Y<sub>6</sub>Co<sub>2</sub> alloy for the primary crystallization reaction at various temperatures.Fig. 9- Local Avrami exponent of Al<sub>86</sub>Cu<sub>6</sub>Y<sub>6</sub>Co<sub>2</sub> amorphous alloy at different rates of heating.

### 3.2.2. Crystallization mechanism

The mechanisms of nucleation and growth processes is usually defined by local Avrami exponent during crystallization. Johnson-Mehl-Avrami (JMA) equation is used to study the kinetic of crystallization of isothermal transformation by [27,28]:

$$\alpha(T) = 1 - \exp[-K(t - \tau)^n] \quad (4)$$

In this equation,  $\alpha(t)$  is the volume fraction of crystallized phase,  $t$  is the time required for the crystallized volume fraction,  $\tau$  is the incubation time,  $K$  is a kinetic coefficient and  $n$  is the Avrami exponent. Handerson extended the JMA equation in non-isothermal conditions in the case the nucleation process occurs during the early stages of the transformation completely and then becomes sluggish [29]:

$$\alpha(T) = 1 - \exp\left[\left(\frac{KT}{\beta}\right)^n\right] \quad (5)$$

This equation can be written as:

$$\ln[-\ln(1 - \alpha)] = -n \ln \beta + \ln K(T) \quad (6)$$

The values of  $n$  can be obtained from the slope of the straight lines derives from plotting  $\ln[-\ln(1 - X)]$  versus  $\ln \beta$  at different temperatures. The amount of Avrami exponent predicts nucleation and growth mechanisms. The mean value of  $n$  which obtained from the straight lines of Fig. 8 at different temperatures (583, 588 and 598 K) are reported. The amounts of Avrami exponent range from 2.06 to 2.17. According to The average value of Avrami exponent ( $n = 2.065 \pm 0.16$ ), the primary crystallization conducts by diffusional growth with decreasing nucleation rate. It is reported that in a number of amorphous Al, the Avrami exponent ranges from 1.6 to 5.0 which depends strongly on the composition [11].

Fig. 9 shows the local Avrami exponent of the Al<sub>86</sub>Cu<sub>6</sub>Y<sub>6</sub>Co<sub>2</sub> amorphous alloy at different rates of heating. The value of local Avrami exponent is generally high at the initial stage of crystallization. At the initial and the final stages of crystallization, the Avrami exponent is inconstant. The value of  $n$  versus crystallized volume fraction are considered in the range ( $0.2 < \alpha < 0.8$ ), due to high error at low and high crystallized volume fraction. Unevenly distributed pre-existing nuclei in the glassy alloy,

and/or an inhomogeneous nucleation of the crystallization process probably leads to abnormal improvement in the local Avrami exponents at high crystallize volume fractions. At the middle stage of crystallization, the local Avrami exponent seems to be constant indicating the growth of the nuclei at a detectable size.

#### 4. Conclusions

The crystallization kinetic and microstructure of the melt-spun amorphous  $\text{Al}_{86}\text{Cu}_6\text{Y}_6\text{Co}_2$  (at %) alloy is investigated by DSC analysis in non-isothermal conditions. The crystallization temperature of the melt-spun alloy is 576 K at 20  $\text{K min}^{-1}$  and crystallization occurs in two stages. Fcc-Al nanocrystals with a mean grain size less than 50 nm are precipitated from an amorphous matrix during the primary crystallization. Different intermetallic compounds including  $\text{Al}_3\text{Y}$ ,  $\text{AlCu}_3$  and  $\text{Al}_{11}\text{Y}_3$  phases and some undefined phases are formed from the residual amorphous phase at 723 K. All DSC peaks move to the higher temperatures with the heating rate advancement. In the DSC curve, there is Glass transition before the first crystallization reaction of the amorphous alloy. Moynihan and Kissinger equations determine the activation energies of the primary crystallization reaction ( $E_a$ ) with a good agreement as  $183.1 \pm 12.4$  and  $173.4 \pm 10.7$   $\text{kJ mol}^{-1}$ , respectively. According to the average Avrami exponent ( $\sim 2.1$ ), the primary crystallization process takes place by diffusional growth with a decreasing nucleation rate.

#### References

- ÖZTÜRK S, SÜNÜL SE, İCİN K. Effects of melt spinning process parameters and wheel surface quality on production of 6060 aluminum alloy powders and ribbons. *Transactions of Nonferrous Metals Society of China*. 2020;30(5):1169-82.
- Dehghani K, Salehi M, Salehi M, Aboutalebi H. Comparing the melt-spun nanostructured aluminum 6061 foils with conventional direct chill ingot. *Materials Science and Engineering: A*. 2008;489(1-2):245-52.
- Salehi M, Dehghani K. Structure and properties of nanostructured aluminum A413.1 produced by melt spinning compared with ingot microstructure. *Journal of Alloys and Compounds*. 2008;457(1-2):357-61.
- Karaköse E, Keskin M. Structural investigations of mechanical properties of Al based rapidly solidified alloys. *Materials & Design*. 2011;32(10):4970-9.
- Katgerman L, Dom F. Rapidly solidified aluminium alloys by meltspinning. *Materials Science and Engineering: A*. 2004;375-377:1212-6.
- Salehi M, Shabestari SG, Boutorabi SMA. Nanostructure and Mechanical Properties of Bulk  $\text{Al}_{86}\text{Ni}_6\text{Y}_6\text{Ce}_2$  Alloy Produced by Hot Consolidation of Amorphous Melt-Spun Flakes. *Metallurgical and Materials Transactions A*. 2014;45(13):6344-51.
- Salehi M, Shabestari SG, Boutorabi SMA. Nanostructure evolution and mechanical properties of rapidly solidified  $\text{Al}_{3}\text{Ni}_3\text{RE}$  (Y, Ce) alloys. *Materials Science and Engineering: A*. 2013;586:407-12.
- Triveño Rios C, Suriñach S, Baró MD, Bolfarini C, Botta WJ, Kiminami CS. Glass forming ability of the Al-Ce-Ni system. *Journal of Non-Crystalline Solids*. 2008;354(42-44):4874-7.
- Wang SH, Bian XF. Effect of Si and Co on the crystallization of Al-Ni-RE amorphous alloys. *Journal of Alloys and Compounds*. 2008;453(1-2):127-30.
- Cuevas FG, Lozano-Perez S, Aranda RM, Caballero ES. Crystallization of amorphous Al-Sm-Ni-(Cu) alloys. *Intermetallics*. 2008; 106537- 112.
- Shen Y, Perepezko JH. Al-based amorphous alloys: Glass-forming ability, crystallization behavior and effects of minor alloying additions. *Journal of Alloys and Compounds*. 2017;707:3-11.
- Wang Y, Liu Y, Li Y, An B, Cao G, Jin S, et al. Crystallization of Al-based Amorphous Alloys in Good Conductivity Solution. *Journal of Materials Science & Technology*. 2014;30(12):1262-70.
- Roy D, Raghuvanshi H. Study on crystallization kinetics of  $\text{Al}_{65}\text{Cu}_{20}\text{Ti}_{15}$  amorphous alloy. *Journal of Non-Crystalline Solids*. 2011;357(7):1701-4.
- Révész Á, Varga LK, Suriñach S, Baró MD. Thermal stability, crystallization kinetics, and grain growth in an amorphous  $\text{Al}_{85}\text{Ce}_5\text{Ni}_8\text{Co}_2$  alloy. *Journal of Materials Research*. 2002;17(8):2140-6.
- Hyun JI, Kim CI, Nam SW, Kim WT, Kim DH. Nanoscale phase separation and microstructure evolution during crystallization in Al-Si-Ni amorphous alloy. *Materials & Design*. 2020;192:108719.
- Salehi M, Shabestari SG, Boutorabi SMA. Nano-crystal development and thermal stability of amorphous Al-Ni-Y-Ce alloy. *Journal of Non-Crystalline Solids*. 2013;375:7-12.
- Kim HS, Hong SI. A model of the ductile-brittle transition of partially crystallized amorphous Al-Ni-Y alloys. *Acta Materialia*. 1999;47(7):2059-66.
- Huang ZH, Li JF, Rao QL, Zhou YH. Primary crystallization of Al-Ni-RE amorphous alloys with different type and content of RE. *Materials Science and Engineering: A*. 2008;489(1-2):380-8.
- Dong Q, Song P, Tan J, Qin XM, Li CJ, Gao P, et al. Non-isothermal crystallization kinetics of a Fe-Cr-Mo-B-C amorphous powder. *Journal of Alloys and Compounds*. 2020;823:153783.
- Gögebakan M, Okumus M. Structure and crystallization kinetics of amorphous Al-Ni-Si alloy. *Materials Science (0137-1339)*. 2009 Jun 1;27(2).
- Inoue A. Stabilization of metallic supercooled liquid and bulk amorphous alloys. *Acta Materialia*. 2000;48(1):279-306.
- Song K, Bian XF, Lv X, Guo J, Li G, Xie M. Correlation between glass-forming ability, thermal stability, and crystallization kinetics of Cu-Zr-Ag metallic glasses. *Materials Science and Engineering: A*. 2009; 87:93- 506.
- Kissinger HE. Variation of peak temperature with heating rate in differential thermal analysis. *Journal of Research of the National Bureau of Standards*. 1956;57(4):217.
- Kissinger HE. Reaction Kinetics in Differential Thermal Analysis. *Analytical Chemistry*. 1957;29(11):1702-6.
- Fatmi M, Ghebouli B, Ghebouli MA, Chihi T, Abdul Hafiz M. The kinetics of precipitation in Al-2.4wt% Cu alloy by Kissinger, Ozawa, Bosswel and Matusita methods. *Physica B: Condensed Matter*. 2011;406(11):2277-80.
- Augis JA, Bennett JE. Calculation of the Avrami parameters

for heterogeneous solid state reactions using a modification of the Kissinger method. *Journal of Thermal Analysis*. 1978;13(2):283-92.

27. Paul T, Loganathan A, Agarwal A, Harimkar SP. Kinetics of isochronal crystallization in a Fe-based amorphous alloy. *Journal of Alloys and Compounds*. 2018;753:679-87.

28. Lu XF, Hay JN. Isothermal crystallization kinetics and melting behaviour of poly(ethylene terephthalate). *Polymer*. 2001;42(23):9423-31.

29. Henderson DW. Thermal analysis of non-isothermal crystallization kinetics in glass forming liquids. *Journal of Non-Crystalline Solids*. 1979;30(3):301-15.